Supplementary Material for

Stick-Slip Dynamics of Moiré Superstructure in Polycrystalline 2D Material Interfaces

Xiang Gao, Michael Urbakh*, Oded Hod

Department of Physical Chemistry, School of Chemistry, The Raymond and Beverly Sackler Faculty of Exact Sciences and The Sackler Center for Computational Molecular and Materials Science, Tel Aviv University, Tel Aviv 6997801, Israel.

*Corresponding author. Email: urbakh@tauex.tau.ac.il

In this supplemental material, we provide additional details regarding the following aspects of the study reported in the main text:

1. Methods

1.1. General description of the model system

The model system is constructed of three layered components: (i) a pristine graphene (PrisGr) bilayer substrate; (ii) a polycrystalline graphene (PolyGr) layer; and (iii) a trilayer *h*-BN stack (see Fig. 1 of the main text). To construct the periodic PrisGr/PolyGr/*h*-BN heterojunction, incorporating the ~1.8% intralayer lattice mismatch between *h*-BN and Gr, the lateral dimensions of the simulation box $(L_x \times L_y)$ are chosen to be approximately 56×56 Gr unit cells, and 55×55 *h*-BN unit cells, where the 56/55 ≈ 1.0182 ratio accounts well for the intrinsic lattice mismatch. The supercells of the pristine Gr and *h*-BN layers are rectangular in shape with their armchair (zigzag) direction lying along the x (y) axis. Given the lattice periods in the zigzag and armchair directions ($a_{\mathrm{Gr}}^{\mathrm{zigzag}} = \sqrt{3}d_{\mathrm{cc}} \approx 2.46$ Å and $a_{\mathrm{Gr}}^{\mathrm{armchair}} = 3d_{\mathrm{cc}} \approx 4.26$ Å), this results in an overall surface area of $23.86 \times 13.78\ \mathrm{nm}^2$. Using the second-generation reactive empirical bond order (REBO) potential [1] and Tersoff potential [2] to describe the intralayer interactions for Gr and *h*-BN, the equilibrium carbon-carbon and boron-nitrogen bond lengths are $d_{\mathrm{cc}} = 1.42039$ Å and $d_{\mathrm{BN}} = 1.44214$ Å, respectively. To reduce residual strain, the equilibrium B-N bond length in the Tersoff potential is increased by 0.28% to $d_{\mathrm{BN}} = 1.446215$ Å with a negligible effect on the calculated elastic properties [3]. The polyGr layer is constructed from two grains, where their grain boundary (GB) seamline lies along the *y*-direction (see Fig. 1(b) of the main text and Fig. S1(a)). The armchair (zigzag) direction of Grain 1 is oriented along the x (y) axis forming Bernal (AB) stacking with the underlying PrisGr bilayer substrate. The lattice of Grain 2 is rotated counterclockwise with respect to that of Grain 1, where the inter-grain misfit angle, θ_{m}, is chosen to allow for applying lateral periodic boundary conditions with minimal residual strain (see Supplementary Methods section of Ref. [4]).

For comparison purposes, some calculations performed in this study were repeated for a homogeneous PrisGr/PolyGr/PrisGr system constructed like the heterogeneous system described above with a PrisGr trilayer replacing the *h*-BN stack. In this case, to avoid commensurate high-friction stacking, the PrisGr trilayer slider is rotated by 38.2° with respect to the underlying PrisGr substrate (see Fig. S1(b)).

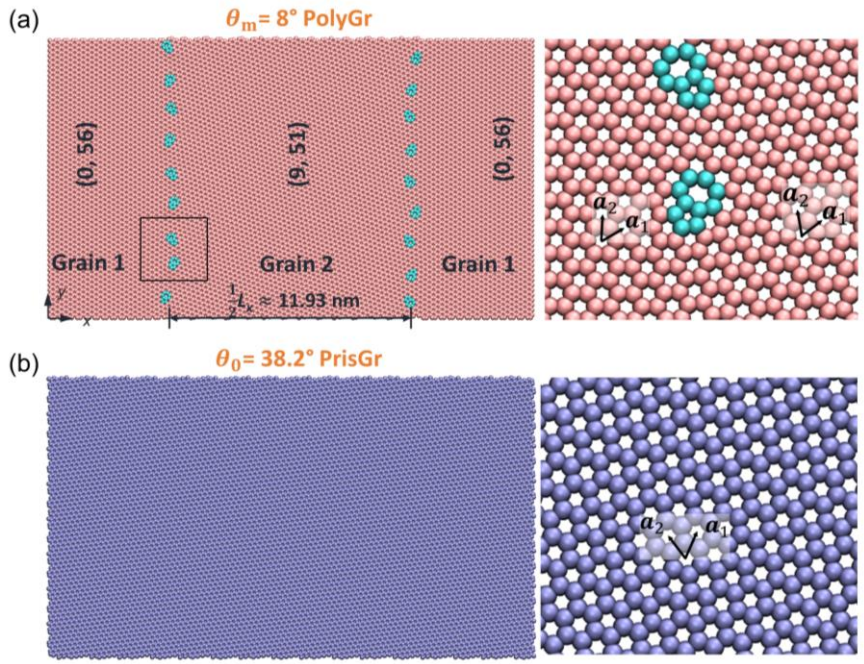

FIG. S1. Atomic structures of PolyGr and PrisGr layer models. (a) PolyGr layer with an inter-grain misfit angle of $\theta_m = 8°$. The pink and cyan spheres represent the hexagonal and the pentagon-heptagon pair atoms, respectively. (b) homojunction PrisGr slider layer rotated by $\theta_0 = 38.2°$ with respect to the underlying PrisGr substrate bi-layer. Zoom-in views, marking the lattice vectors (green) for the different grains, are provided on the right-hand side of each panel.

1.2. Relaxed topography of the PolyGr layer

Following structural relaxation, the PolyGr layer renders complex out-of-plane topography, exhibiting a series of upward/downward protrusions in the vicinity of the pentagon-heptagon GB dislocations, and pronounced moiré superstructures within the grains. This results from the balance between intralayer interactions and interlayer interactions with the underlying PrisGr layers and the overlying *h*-BN layers. Below 10°, as the inter-grain misfit angle (θ_{m}) increases, the GB protrusion density increases (see Fig. S2(a)-S2(b)) and their height decreases, e.g. from 0.85 ± 0.04 Å at $\theta_{\mathrm{m}} = 1.8°$ to 0.46 ± 0.17 Å at $\theta_{\mathrm{m}} = 8°$, on average. For inter-grain misfit angles larger than 10°, the dislocation density further increases such that the pentagon-heptagon pairs partially or fully connect with their neighboring counterparts by sharing a C-C bond, a hexagon ring, or a pair of mutual edge atoms. This leads to a mutual cancellation of local strains, suppressing the corrugation of the protrusions. For certain cases, e.g. $\theta_{\mathrm{m}} = 21.8°$, the in-plane strain cancellation results in a flat GB (see Fig. S2(c), S2(f)). Further information regarding the structural and topological properties of graphene GBs can be found in Ref. [5].

The moiré superstructure formed between the graphene surface of the two grains and each of its surrounding hexagonal lattices can be described as a triangular superlattice with periodicity λ and angular orientation ψ, given by the following expressions [6]:

$$\lambda = \frac{(1+\delta)a_{\mathrm{cc}}}{\sqrt{2(1+\delta)(1-\cos\theta_T)+\delta^2}},$$

$$\psi = \tan^{-1}\frac{(1+\delta)\sin\theta_T}{(1+\delta)\cos\theta_T - 1}, \tag{S1}$$

where δ is the mismatch between the lattice constants of each pair of hexagonal lattices, a_{cc} is the period of graphene lattice, and θ_T is the twist angle between the layers. As Grain 1 is Bernal stacked with the underlying graphitic substrate layers, its moiré superstructures originate only from its incommensurate interface with the overlying *h*-BN layer. Considering a lattice mismatch of $\delta = 0.0182$, the moiré supercell dimensions for the chosen *h*-BN stack orientation ($\theta_T = 0°$) are 23.86×13.78 nm^2. Hence, as shown in Fig. S1, in our model system Grain 1 accommodates a full moiré period along the y-direction and half of a moiré period along the x (sliding) direction.

The situation for Grain 2 is more involved as it needs to comply with commensurability requirements enforced by its two adjacent layers. For the inter-grain misfit angle of $\theta_{\mathrm{m}} = 8°$

discussed in the main text, the moiré superstructure periods at its interfaces with the *h*-BN and PrisGr layers are roughly equal (~ 1.76 nm) yielding a hexagonal pattern with a small rotation away from $\psi = 0°$ (see Fig. 1(c) of the main text and Fig. S2(e)). Due to the relatively large twist angle, this hexagonal superstructure incorporates out-of-plane surface undulations with a typical period much smaller than that of the full moiré pattern. Reducing the inter-grain mismatch angle to $\theta_{\mathrm{m}} = 1.8°$, results in differing moiré periods of 6.85 nm and 7.83 nm, with the adjacent *h*-BN and PrisGr layers, respectively. As a consequence of these competing interests, a deformed hexagonal superstructure is formed with a small rotation away from $\psi = 0°$ (Fig. S2(d)). In this case, due to the small twist angle, no short-wave-length undulations are obtained. For large inter-grain mismatch angles (e.g. $\theta_{\mathrm{m}} = 21.8°$), the moiré periods formed between Grain 2 and its adjacent *h*-BN and PrisGr layers are very similar and as small as 0.66 nm and 0.65 nm, respectively. Since these values approach the size of the atomic lattice, the resulting moiré superstructure becomes nearly unnoticeable, and Grain 2 remains nearly flat (Fig. S2(f)). In general, the smaller moiré periods on Grain 2 are characterized by less significant in-plane strain/stress effects than those on Grain 1 (see SM Fig. S1 of Ref. [7]).

Notably, for the homogeneous graphitic systems considered herein we deliberately chose a large twist angle ($\theta_T = 38.2°$) between the PolyGr surface and its adjacent slider PrisGr layer to avoid a-priori high-friction configurations. This results in very small moiré periods of 0.65 nm and 0.48 nm over Grain 1 and Grain 2, respectively, for an inter-grain mismatch angle of $\theta_{\mathrm{m}} = 8°$. Similarly, moiré periods of 0.65 nm and 0.86 nm over Grain 1 and Grain 2, respectively, are obtained for an inter-grain mismatch angle of $\theta_{\mathrm{m}} = 21.8°$. Hence, the corresponding moiré superstructures are very minor and their induced in-plane stress effects are negligible.

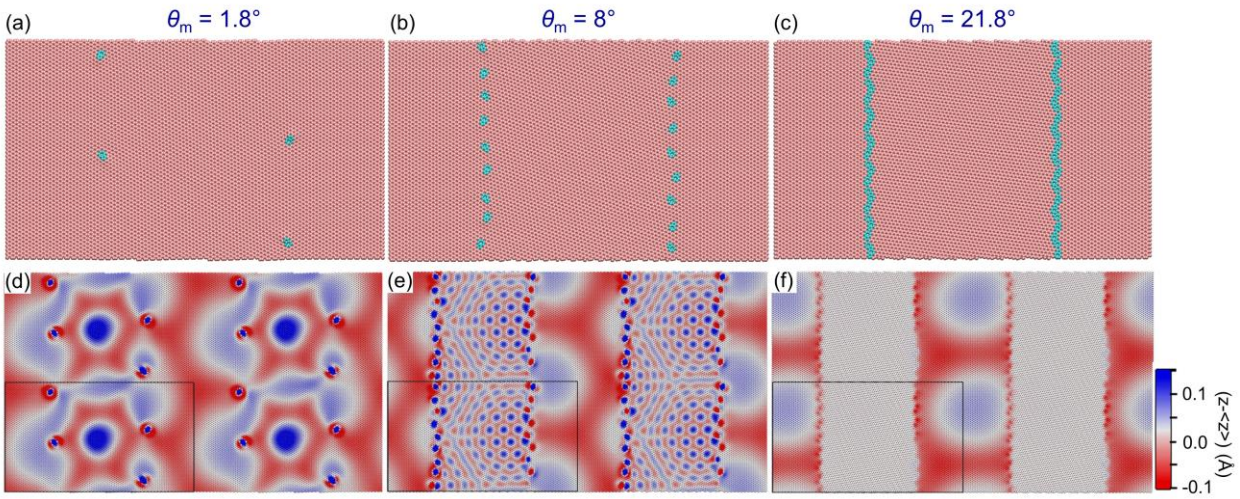

FIG. S2. Relaxed topographies of PolyGr layers with different inter-grain mismatch angles. (a)-(c) Atomic structures of PolyGr with inter-grain mismatch angles of (a) $\theta_m = 1.8°$, (b) $\theta_m = 8°$, and (c) $\theta_m = 21.8°$. Atoms residing in a hexagonal environment are colored in pink, whereas atoms at lattice dislocation sites are colored in cyan. (d)-(f) GB corrugation maps for (d) $\theta_m = 1.8°$, (e) $\theta_m = 8°$, and (f) $\theta_m = 21.8°$. The atoms are color according to their out-of-plane displacement with respect to the average height of the PolyGr layer according to the color bar on the right of panel (f). We note that in order to visualize the moiré structures, the color bar range is limited to -0.1-0.15 Å, whereas the GB corrugation exceeds these values at some points. The black frames outline the primary simulation supercell and the rest are periodic replicas presented to clearly demonstrate the moiré superstructures.

1.3. Simulation protocol

All simulations were carried out using the LAMMPS package [8]. To describe the intralayer interatomic interactions within each Gr and *h*-BN layer, we employed the REBO [1] and the Tersoff [2] potentials, respectively. For the interlayer interactions we adopted our registry-dependent interlayer potential (ILP) [9-13]. Recently, the combination of the REBO intralayer potential and the ILP was shown to provide GB energies and topographies consistent with DFT calculations and experimental observations [5,14-16].

The PolyGr/PrisGr substrate was first minimized and annealed before the *h*-BN layers were placed atop it. The detailed relaxation procedure for the PolyGr/PrisGr can be found in Ref. [4]. After combining the relaxed PolyGr/PrisGr substrate with the *h*-BN slider, the whole system was relaxed for 200 ps under zero temperature damped dynamics simulation. Initial configurations under different normal loads were prepared by increasing the external force applied to the atoms of the top layer, which was kept rigid (allowing only for vertical rigid body motion), in a stepwise manner. After each such increment a relaxation process of 100 ps zero temperature damped dynamic simulation followed. The applied external force was taken to be in the range of -0.01–0.08 nN/atom, corresponding to a normal load range of -0.4–2.9 GPa. The initial configurations for room temperature (300 K) were generated by equilibrating the corresponding zero temperature configurations for 200 ps under Langevin thermostats.

The simulation protocol for dynamic sliding simulations was similar to that used in our previous study on PrisGr/PolyGr/PrisGr homojunctions [4]. The *h*-BN slider was modeled by a three-layer stack, where the top layer was rigidly shifted in the x-direction at a constant sliding velocity of $v_0 = 5\ \mathrm{m/s}$ allowing only for its rigid body vertical motion. The remaining two *h*-BN layers were flexible to follow the dynamics based on the abovementioned force-fields (see Fig. 1 of the main text). Similarly, the bottom graphene substrate layer was kept fixed during the dynamics and both the PolyGr and the middle PrisGr layers were fully flexible. To remove the heat generated during the shear motion, viscous damping with a damping coefficient of $\eta = 1.0$ ps^{-1} was applied to the atoms in the second *h*-BN layer (l_2) and the flexible PrisGr (l_5) in all three directions. The corresponding damping terms are given by:

$$\mathbf{f}_{\mathrm{damp}}^{i,l_2}(t) = -m^i\eta\left[v_x^{i,l_2}(t) - v_0\right]\hat{\mathbf{x}} - m^i \sum_{\alpha=y,z} \eta\, v_\alpha^{i,l_2}(t)\hat{\boldsymbol{\alpha}},\ \ m^i = m_{\mathrm{B}} \text{ or } m_{\mathrm{N}},$$

$$\mathbf{f}_{\mathrm{damp}}^{i,l_5}(t) = -m_{\mathrm{C}} \sum_{\alpha=x,y,z} \eta v_{\alpha}^{i,l_5}(t)\, \hat{\boldsymbol{\alpha}}, \tag{S2}$$

where $m_{\mathrm{C}}, m_{\mathrm{B}}$, and m_{N} are the atomic masses of carbon, boron, and nitrogen atoms, respectively, $v_{\alpha}^{i,l_k}(t)$ is the α Cartesian velocity component of the i^{th} atom in layer l_k ($k = 2$ or 5) at time t, and $\hat{\boldsymbol{\alpha}} = \hat{\mathbf{x}}, \hat{\mathbf{y}}, \hat{\mathbf{z}}$ are the unit vectors in the x, y and z directions, respectively. The first term on the right-hand side of the damping equation for layer l_2 implies that the damping in the shear direction of this layer is applied to the relative atomic velocities with respect to the driving velocity v_0, accounting for the fact that in realistic scenarios viscous dissipation is caused by the internal degrees of freedom of the sheared bodies. We note that the viscous damping terms are required as our model system thickness is finite, such that in their absence unphysical vibrational backscattering into the interfacial region from the artificial model system boundaries would occur. The viscous damping terms thus mimic energy dissipation via long-lived vibrational excitations that propagate away from the frictional interface into the supporting bulk regions present in realistic interfaces. Since we are mainly concerned with the overall energy that such vibrations carry away rather than their specific dynamics within the bulk regions, the use of viscous damping terms is well justified as long as the results do not strongly depend on the chosen damping rate (see Ref. [5]).

In room temperature simulations, Langevin thermostats with the same damping settings as those of the zero temperature simulations were applied to layers l_2 and l_5. Since the random thermostat forces are not correlated between the various atoms to which they are applied, the total random force applied at each time step does not exactly nullify, leading to a slow random walk of the center of mass of the thermostatted layer. Therefore, to avoid artificial contributions to the calculated friction, the total random force of each damped layer was cancelled out by subtracting an equal part of it from each atom within the layer at each time step. Typically, the dynamic simulations lasted for 2-3 ns at zero temperature and 6-10 ns at room temperature so as to achieve sufficiently long steady state lateral force traces required for the calculation of the average friction. Representative lateral force traces and convergence validation of the friction calculations are discussed in detail in Sec. 2 below.

1.4. Quasistatic simulations

In the quasistatic simulations, each minimization cycle included a 0.02 Å displacement of the top layer in the *x* direction followed by geometry relaxation using the FIRE algorithm [17,18] with a force tolerance of 1×10^{-4} eV/Å. The process was repeated up to a total displacement of 4.34 Å (217 displacement steps), corresponding to a full period along the armchair *h*-BN direction. The convergence of the extracted quasi-static friction with the optimization force tolerance is shown in Fig. S3. As the force tolerance is reduced, the calculated friction force gradually approaches the dynamic simulation result obtained at the lowest shear velocity considered $(0.1\ \mathrm{m/s})$. For a force tolerance of 1×10^{-4} eV/Å, the relative difference with respect to the dynamic result is ~6.7%. Naturally, part of this difference originates from dynamic effects induced by the finite sliding velocity of the latter. The above analysis thus validates convergence of the quasistatic results with respect to the optimization force-tolerance parameters and the overall consistency of our approach.

Similar to the dynamic calculations, during each quasi-static geometry relaxation step, the bottom graphene layer was kept fixed, and the top *h*-BN layer was allowed to rigidly relax only along the vertical direction. Due to technical details of the LAMMPS code, the latter was performed by artificially setting the atomic masses of boron and nitrogen in the top layer to be identical (here, for simplicity, taken to be the mass of a carbon atom) and applying to all of them a uniform vertical force equal to the corresponding average force acting on all atoms in this layer at each iteration of the FIRE optimization procedure.

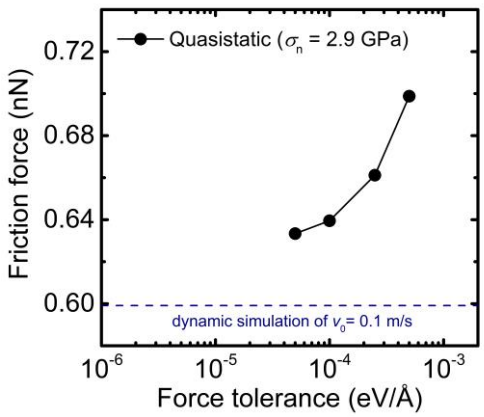

FIG. S3. Convergence test of the quasi-static friction force calculation with respect to the optimization force tolerance applied in the FIRE algorithm.

2. Lateral Force Traces and Friction Force Calculation

The friction force results presented in Fig. 3 of the main text are calculated by averaging the lateral forces acting on the top slider layer over several sliding periods. The number of periods was taken to be sufficiently large to assure convergence of the average value and reduction of thermally induced fluctuation effects. Figure S4 presents representative force traces for zero and room temperature simulations at different normal loads. The lateral force traces exhibit clear periodic patterns with a period of $t_0 = \frac{a_{h-\mathrm{BN}}^{\mathrm{armchair}}}{v_0} = \frac{4.33865\ \text{Å}}{5\ \mathrm{m/s}} = 86.77$ ps, corresponding to sliding over one armchair period of *h*-BN. To calculate the friction forces, we averaged over time windows of $3t_0$ and $40t_0 - 60t_0$ for the zero and room temperature traces, respectively. The larger time window chosen for the room temperature traces was required to average out thermal fluctuations induced errors. Figure S5 demonstrates the convergence of the calculated zero temperature friction force with the length of the averaging window for different normal loads. Once steady state is obtained, above a time window of $3t_0$, the zero-temperature friction force calculation is well converged for all normal loads considered. Similarly, for the room temperature simulations the average friction force converges at a time window of $40t_0 - 60t_0$, depending on the specific trace (see Fig. S6). The error bars for the heterojunctions at 300 K shown in Fig. 3(c)-3(d) of the main text are set as standard deviations of temporal friction force averages calculated using a running averaging window of $10t_0$.

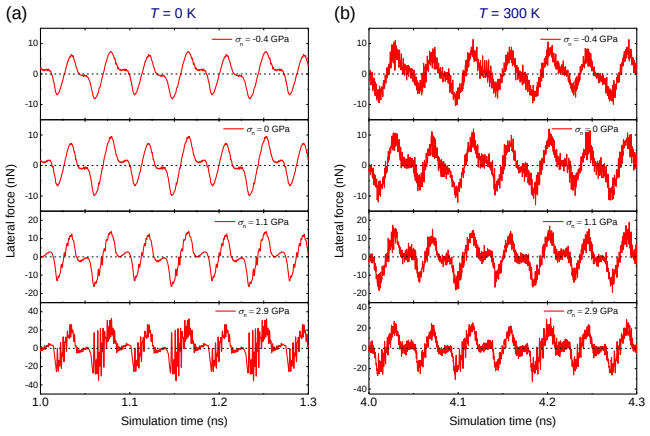

FIG. S4. Representative lateral force traces at steady state for (a) zero temperature and (b) room temperature under normal loads of -0.4, 0, 1.1, and 2.9 GPa from top to bottom in each column.

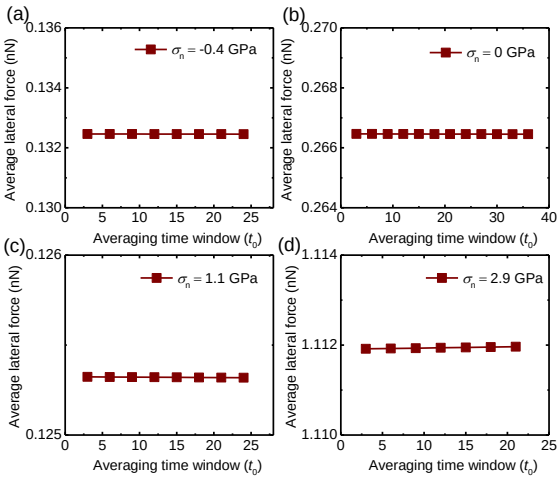

FIG. S5. Convergence of the friction force estimation with the averaging time window for zero temperature simulations performed under normal loads of (a) -0.4 GPa, (b) 0 GPa, (c) 1.1 GPa, and (d) 2.9 GPa. For all time windows, averaging started after steady-state is well reached, namely after $3t_0$.

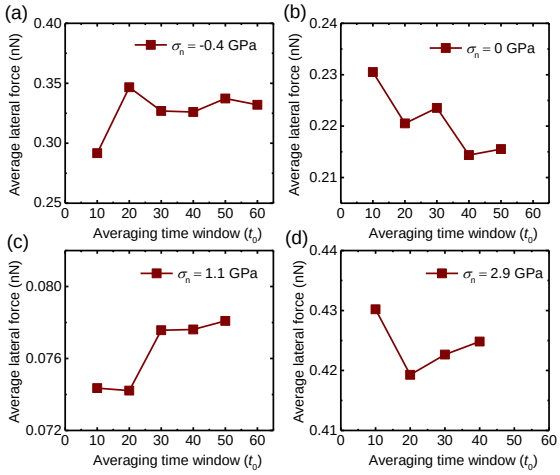

FIG. S6. Convergence of the friction force estimation with the averaging time window for room temperature simulations performed under normal loads of (a) -0.4 GPa, (b) 0 GPa, (c) 1.1 GPa, and (d) 2.9 GPa. For all time windows, averaging started after steady-state is well reached, namely after $20t_0$.

3. Frictional Dissipation Analysis

3.1. General power balance at steady state

At steady state, the system achieves a general power balance ($p_{\text{in}} = p_{\text{diss}}$) between the input from the slider (p_{in}) and the total dissipation through viscous damping ($p_{\text{diss}} = F_f \cdot v_0$, where F_f is the friction force and v_0 is the shear velocity). Considering zero-temperature simulations, where thermal noises are absent, the total dissipation power p_{diss} can be calculated according to the viscous damping scheme in Eq. S2 as follows:

$$p_{\text{diss}} = p_{\text{diss}}^{l_2} + p_{\text{diss}}^{l_5},$$

$$p_{\text{diss}}^{l_2} = \sum_i^{N_{l_2}} m^i \eta \left(\langle \left[v_x^{i,l_2}(t) - v_0 \right]^2 \rangle + \sum_{\alpha=y,z} \langle v_\alpha^{i,l_2}(t)^2 \rangle \right), m^i = m_{\text{B}} \text{ or } m_{\text{N}} \qquad \text{(S3)}$$

$$p_{\text{diss}}^{l_5} = m_{\text{C}} \eta \sum_i^{N_{l_5}} \sum_{\alpha=x,y,z} \langle v_\alpha^{i,l_5}(t)^2 \rangle,$$

where $m_{\text{C}}, m_{\text{B}}$, and m_{N} are the atomic masses of carbon, boron, and nitrogen atoms, respectively; the superscript l_2, and l_5 represent the two damped layers (see Fig. 1 of the main text); $N_{l_{k=2,5}}$ is the number of atoms in layer l_k; $\eta = 1.0$ ps^{-1} is the damping coefficient; $v_\alpha^{i,l_k}(t)$ is the α Cartesian velocity component of the i^{th} atom in layer l_k at time t, and $\langle \cdot \rangle$ denotes a steady-state temporal average. Figure S7 presents a comparison of p_{in} and p_{diss} at steady-state verifying that general power balance is indeed achieved.

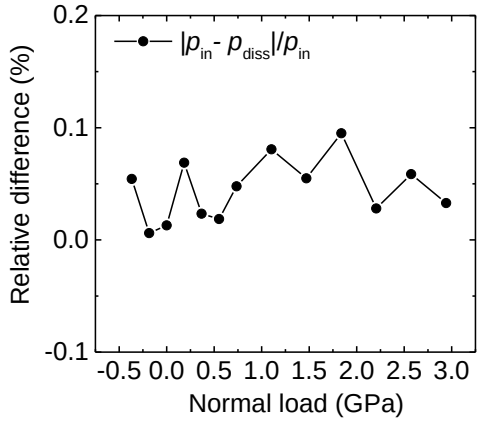

FIG. S7. General power balance between p_{in} and p_{diss} during zero temperature simulations. Plotted is the relative difference (in percent), $\frac{|p_{\text{in}} - p_{\text{diss}}|}{|p_{\text{in}}|} \times 100$, as a function of normal load.

3.2. Comparison of energy dissipation behaviors in the two damped layers

In Fig. 2(c) of the main text, we discussed the directional dissipation components of the system, where each was summed over the corresponding components in the two damped layers, PrisGr layer l_5 and *h*-BN layer l_2. In Fig. 2(a)-2(b) of the main text, we only provided the distributions of power dissipation density for layer l_5. We opted to do this because layer l_2 demonstrates very similar qualitative load dependence of the directional dissipated power (Eq. S3) with some minor quantitative variations. For completeness, we present in Fig. S8 the distributions of power dissipation density for layer l_2. Notably, PrisGr layer l_5 contributes ~55%-80% of the total power dissipation.

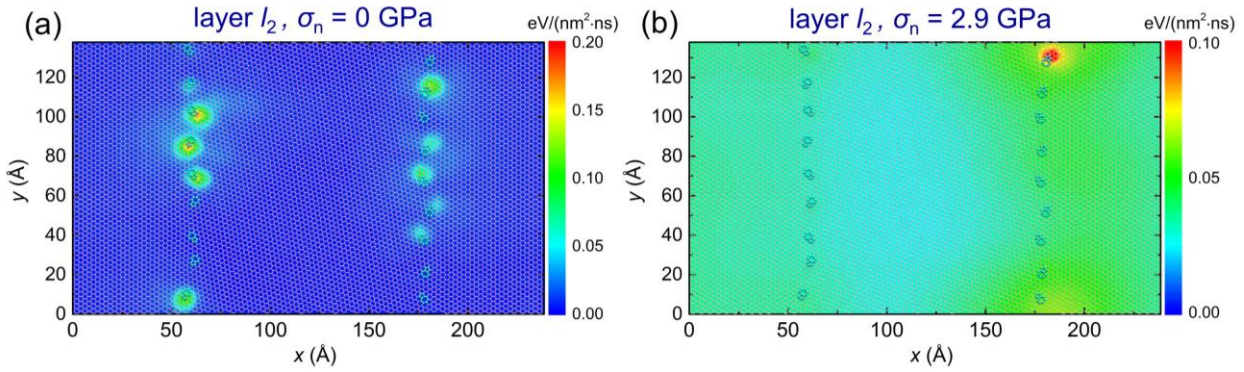

FIG. S8. 2D maps of the time-averaged dissipation power density for the dissipative layer l_2 of the *h*-BN/PolyGr heterojunction with $\theta_m = 8°$ under (a) zero normal load and (b) a normal load of 2.9 GPa. The geometric configuration of the PolyGr layer is superimposed on the 2D maps. Carbon atoms belonging to pentagon-heptagon and hexagonal lattice regions are present by cyan balls and pink bonds, respectively. The dissipation power density distribution maps are calculated by averaging over unit cells of dimensions $a_{Gr}^{armchair} \times a_{Gr}^{zigzag}$, i.e. 4.26×2.46 Å^2.

3.3. Energy dissipation analysis for the flat *h*-BN/PolyGr heterojunction with $\theta_m = 21.8°$

For the *h*-BN/PolyGr heterojunction with flat GBs of $\theta_m = 21.8°$, the directional dissipation power components are shown in Fig. S9. It is seen that the *x*-direction component, which grows with normal load, plays the dominant role in the total energy dissipation throughout the load range considered. Moreover, Fig. S10 demonstrates that the energy dissipation mainly originates from Grain 1 (where significant moiré superstructures appear) at both low and high normal loads. Due to the lack of dynamic buckling of GB protrusions, a monotonic increase of the dissipated power with the normal load is obtained, originating from the dynamic moiré instability mechanism (see Movie 5).

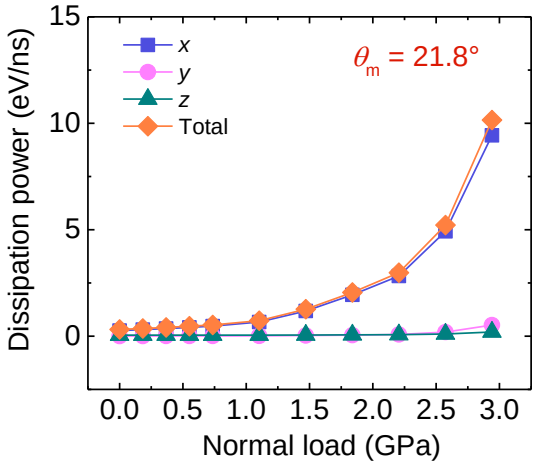

FIG. S9. Directional components of the energy dissipation power as a function of normal load for the flat GB *h*-BN/PolyGr heterojunction with $\theta_m = 21.8°$ at zero temperature.

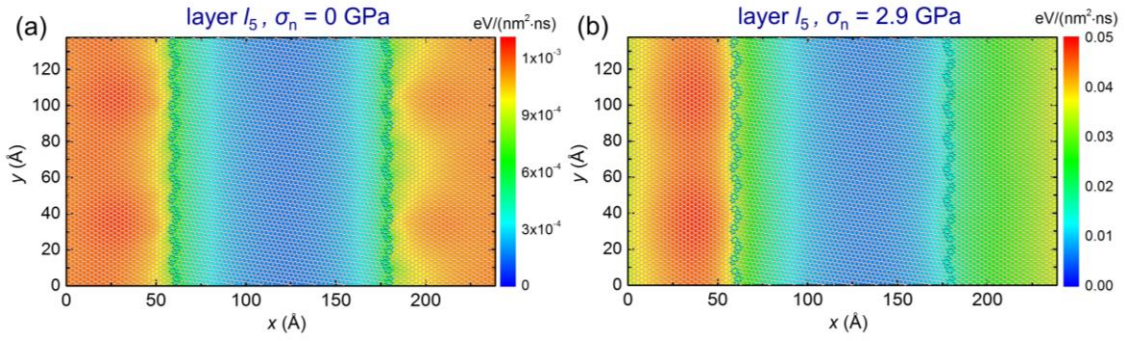

FIG. S10. 2D maps of the time-averaged dissipation power density for the flat GB *h*-BN/PolyGr heterojunction with $\theta_m = 21.8°$. Distribution of dissipation power density for dissipative layer l_5 under (a)

zero normal load and (b) a normal load of 2.9 GPa. The geometric configuration of the PolyGr layer is superimposed on the 2D maps. Carbon atoms belonging to pentagon-heptagon and hexagonal lattice regions are present by cyan balls and pink bonds, respectively. The dissipation power density distribution maps are calculated by averaging over unit cells of dimensions $a_{\mathrm{Gr}}^{\mathrm{armchair}} \times a_{\mathrm{Gr}}^{\mathrm{zigzag}}$, i.e. 4.26×2.46 Å^2 (see Sec. 1 above).

3.4. Energy dissipation analysis for PolyGr homojunctions

Unlike the case of PolyGr heterojunctions, the corresponding homojunctions investigated do not exhibit significant moiré superstructures due to the large misfit angles chosen between the bottom slider layer l_3 and the two grains of layer l_4 (see Fig. 1 of the main text). Therefore, the moiré effects on energy dissipation are expected to be negligible in this case.

For the PolyGr homojunction with $\theta_{\mathrm{m}} = 8°$, Fig. S11(a) reports the load dependence of the directional dissipation components at zero temperature. Similar to the corresponding heterojunction case, in the low normal load range (<1.5 GPa) the energy dissipation is dominated by the out-of-plane component and shows a nonmonotonic load dependence. The high dissipation sites are the GB protrusions that undergo strong dynamic snap-through buckling (Fig. S11(b)) [4].

As expected, in the high normal load regime (>1.5 GPa) the snap-through buckling mechanism is suppressed. Furthermore, unlike the case of PolyGr heterojunctions, since the energy dissipation in the grains area of the PolyGr homojunction remains very low (see Fig. S11(c)), all directional dissipation components show negligible dependence on the normal load in this regime (Fig. S11(a)).

For the homojunction with flat GBs of $\theta_{\mathrm{m}} = 21.8°$, where both GB protrusions and moiré superstructures frictional mechanisms are absent, the directional energy dissipation components remain very low throughout the studied range of normal loads (see Fig. S12).

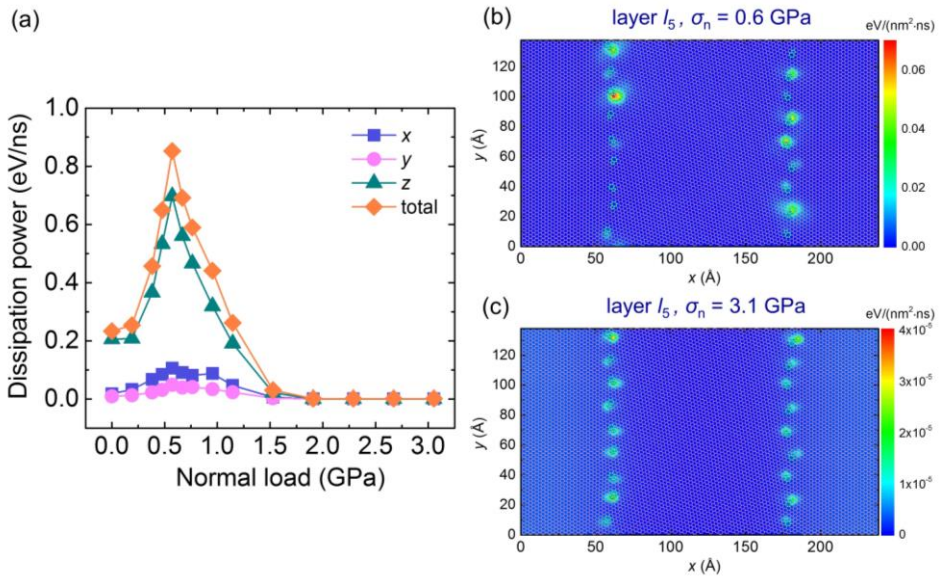

FIG. S11. Energy dissipation characteristics for the PolyGr homojunction with a GB misfit angle of $\theta_m = 8°$ at zero temperature. (a) Energy dissipation power component in each Cartesian direction and their sum as a function of normal load. (b)-(c) 2D maps of energy dissipation power density in the damped PrisGr layer l_5 under (b) a normal load of 0.6 GPa and (c) a normal load of 3.1 GPa. The dissipation power density distribution maps are calculated by averaging over unit cells of dimensions $a_{Gr}^{armchair} \times a_{Gr}^{zigzag}$, i.e. 4.26×2.46 Å^2 (see Sec. 1 above). The results in panel (a) below 2.0 GPa normal load and the results in panel (b) are taken from Ref. [4], the latter is replotted for larger cells.

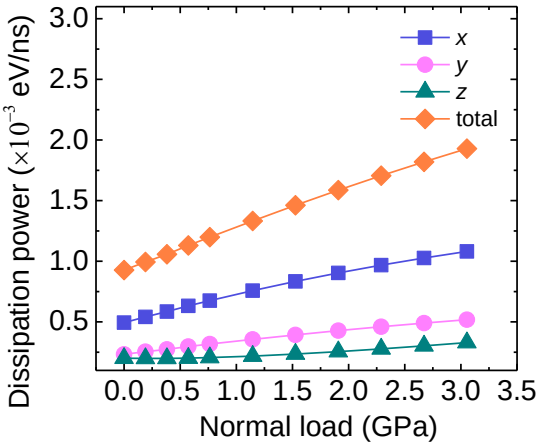

FIG. S12. Normal load dependence of the energy dissipation power along each Cartesian direction (blue, pink, and green) and their sum (orange) for the PolyGr homojunction with a GB misfit angle of $\theta_m = 21.8°$ at zero temperature.

4. Effect of Grain Boundary Separation on the Moiré Stick-Slip Phenomenon

In the main text, the PolyGr surface consisted of two grain boundaries, separated by a distance that accommodates half of the larger moiré superstructure period along the sliding (x) direction in Grain 1 (see Fig. 1 of the main text). To evaluate the effect of grain boundary separation in general and the difference between having fractional or integer numbers of moiré superstructures, we present here results for a system where the x-length of Grain 1 is increased to ~23.9 nm, accommodating a full moiré period (see Fig. S13(a)). The enlarged system shows qualitatively similar moiré stick-slip motion (see Movie 4) with reduced friction forces, especially at the high normal load regime, where stick slip dynamics dominates (see Fig. S13(b)). We attribute this difference to the fact that in the present case, less in-plane stress variations are required to maintain interfacial commensurability over Grain 1 during sliding, thus reducing energy dissipation along this channel.

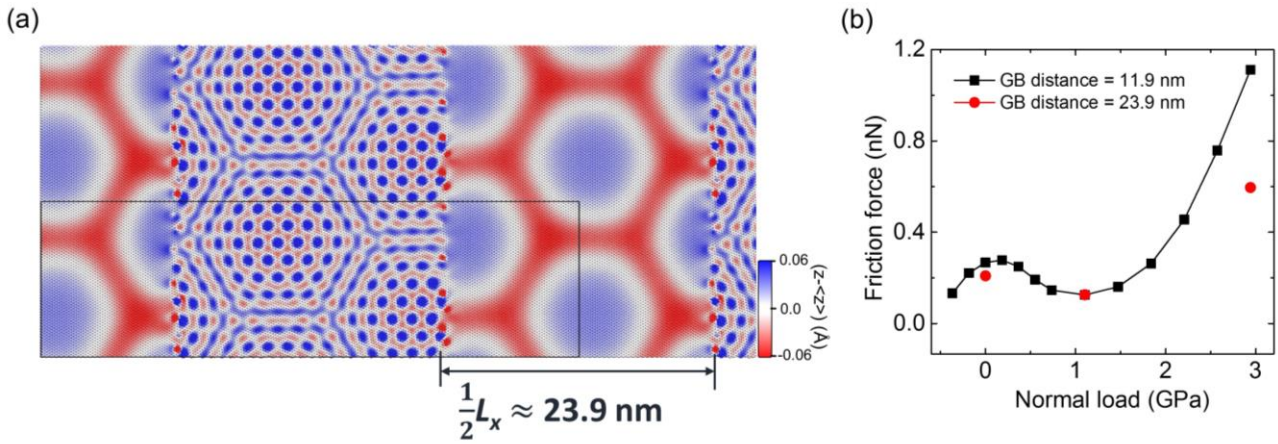

FIG. S13. Effect of grain boundary separation on moiré stick-slip motion. (a) a 2D topography map of the enlarged PolyGr layer with $\theta_m = 8°$. The black frame outlines the primary simulation box. (b) Comparison of friction-load dependence for the original (black squares, see also Fig. 3(a) of the main text) and enlarged (red circles) systems at zero temperature.

5. Interfacial Commensurability Characterization using the Registry Index

To quantitatively characterize the commensurability of the *h*-BN/PolyGr interface, we calculate the global registry index (GRI) in the PolyGr layer, which falls in the range of [0,1] with 0 and 1 corresponding to the most commensurate (AB stacking with Boron atop carbon) and most incommensurate (AA stacking) stacking modes, respectively[19,20]. As shown in Fig. S14, as the normal load increases the entire heterogeneous interface becomes more commensurate, consistent with the stronger in-plane strain effect, where C-C bonds stretch or compress to better match the overlying *h*-BN lattice [3]. We note that the GRI curves reproduce well the interlayer energy profiles at both normal loads considered (see Fig. 4(e) of the main text) down to fine details, indicating that geometric considerations dominate the interlayer sliding energy physics.

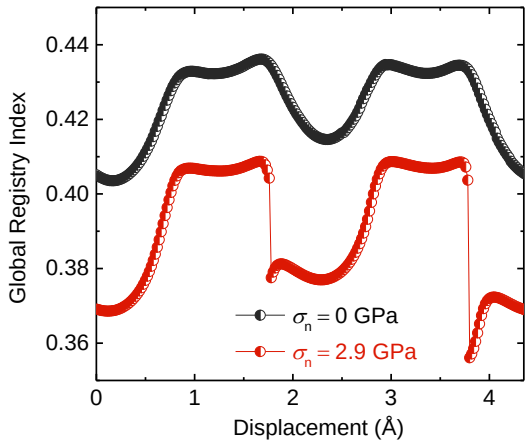

FIG. S14. Global registry index as a function of slider displacement under zero and 2.9 GPa normal loads for the system presented in Fig. 1 of the main text simulated under quasistatic conditions.

6. Lateral Motion of Moiré Triple Junctions

The dynamic translation of moiré superstructures can be characterized by tracking the moiré triple junctions, i.e. the vertices of intersecting moiré grooves separating three adjacent moiré patterns (see Fig. S15(a)). We limit our discussion to zero temperature simulations, where clear moiré triple junction trajectories can be extracted, free of thermal fluctuation effects. Based on the direction of the connected zigzag grooves, the triple junctions are marked as left or right triple junctions, as shown in Fig. S15(a). To track the motion of the triple junctions we use a height criterion to define the group of atoms that constitutes each junction and average over their spatial positions at each time step. This is enabled since the triple junction region is somewhat lower in height from its surrounding.

Before the triple junction reaches the GB, the moiré superstructure moves opposite to the direction of motion of the slider with a velocity given by $v_{\mathrm{m}} = \frac{\lambda_x}{a_{h-\mathrm{BN}}^{\mathrm{armchair}}} \times v_0 = \frac{23.86\ \mathrm{nm}}{4.3386\ \text{Å}} \times 5\ \mathrm{m/s} = 275\ \mathrm{m/s}$, where λ_x is the full moiré period in the sliding direction, $a_{h-\mathrm{BN}}^{\mathrm{armchair}}$ is the corresponding atomic lattice periodicity, and v_0 is the slider velocity.

Fig. S15(b)-S15(d) presents the trajectories of four triple junction locations at increasing normal load. At zero normal load (Fig. S15(b)), the trajectories are relatively smooth demonstrating no apparent stick-slip behavior (see also Supplementary Movie 1). Their velocities (estimated from the slope averages of the corresponding linear trace sections) are ~340 m/s for the left triple junctions and ~300 m/s for the right triple junctions, somewhat higher than the moiré superstructure velocity of $v_{\mathrm{m}} = 275\ \mathrm{m/s}$. We attributed these differences to in-plane stresses that develop within the PolyGr layer due to the presence of GBs and the fact that Grain 1 does not accommodate a full moiré period. For an intermediate normal load of 1.5 GPa (Fig. S15(c)), oscillations occur when the right triple junctions reach GB 2 and new left triple junctions seed near GB 1. Here, the translation velocities for the left and right triple junctions are ~290 m/s and ~280 m/s, respectively, close to the reference velocity, v_{m}. In the vicinity of GB 2 the right triple junction accelerates to ~1.38 km/s until it collides with the GB. Such high incident velocity causes back reflection and subsequent oscillations. Under a high normal load of 2.9 GPa (Fig. S15(d)), the incident velocity of the right triple junctions further grows to ~2.64 km/s resulting in even more pronounced oscillations (See Supplementary Movie 3). These oscillations correspond to the "stripes" pattern in the average $\bar{\sigma}_{xx}$ stress component evolution map appearing in Fig. 5(b) of the

main text. This behavior is a clear manifestation of the superstructure stick-slip dynamics and the ramification of the triple junctions impact upon the GB on the frictional energy dissipation.

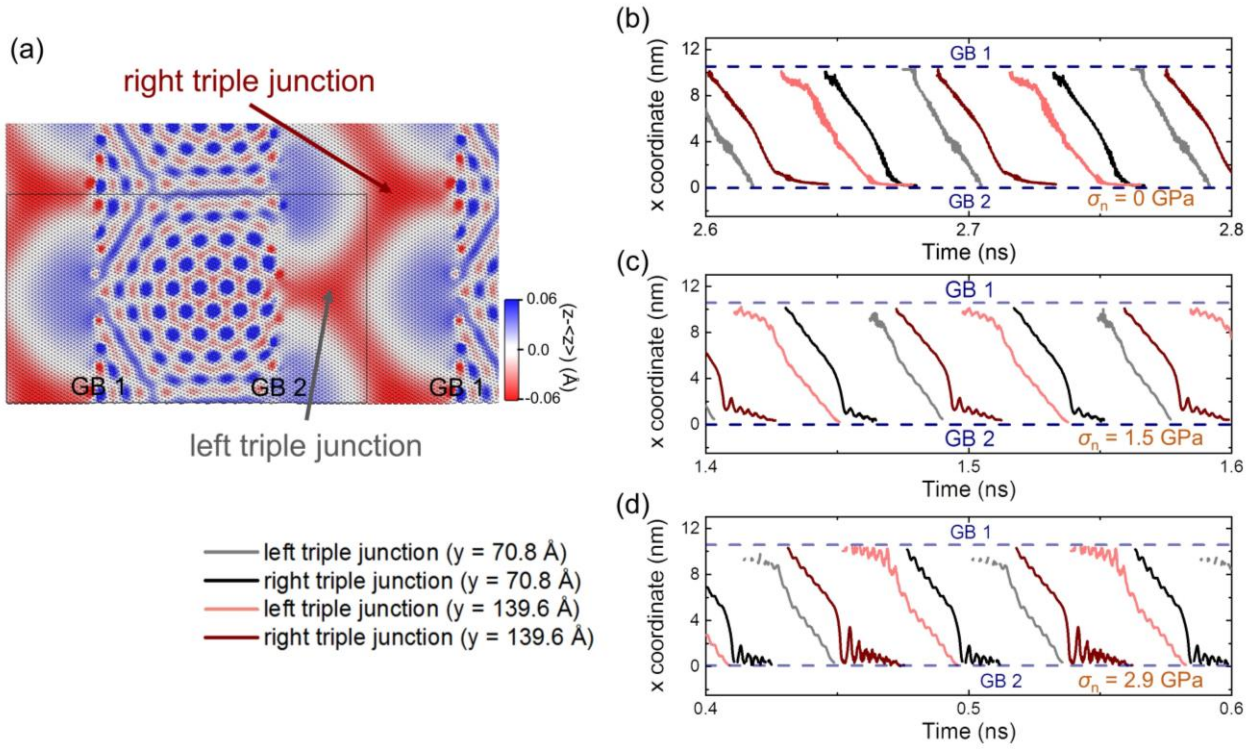

FIG. S15. Motion of moiré triple junctions on Grain 1. (a) Snapshot height map of Grain 1 showing the left and right triple junctions under a normal load of 2.9 GPa. The black frame denotes the primary simulation supercell; the rest are periodic replicas. (b)-(d) Average locations of the triple junctions as a function of time at zero temperature under normal loads of (a) 0 GPa, (b) 1.5 GPa, and (c) 2.9 GPa and a slider velocity of $v_0 = 5$ m/s. The dashed blue lines in panels (b)-(d) mark the position of the two GBs.

7. Stress and Energy Evolution During Moiré Stick-Slip Motion

7.1. Moiré superstructures, atomic stress distributions, and total potential energy

To shed more light on the role of in-plane stress on the discovered frictional mechanism we plot in Fig. S16 several moiré superstructure (a)-(c) snapshots obtained under an external load of 2.9 GPa (panels (b) and (c) are also shown in Fig. 4(a)-4(b) of the main text) and the corresponding lateral stress distributions (d)-(f) in the sliding direction. The elevated (blue) regions appearing in Grain 1 in the top panels represent areas with elongated C-C bonds (hot colors in the lower panels), which are stretched to enhance the commensurability with the adjacent *h*-BN layer, whereas the red grooves are moiré domain walls exhibiting compressive stress (cold colors in the lower panels). Fig. S16 demonstrates that before a moiré triple junction hits the GB the overall lateral stresses in Grain 1 are relatively small. As the junction approaches the GB, lateral tensile stress develops reaching a maximum when the triple junction abruptly eliminates. Further motion of the slider results in an eventual release of this stress as a new triple junction seeds at the opposite GB.

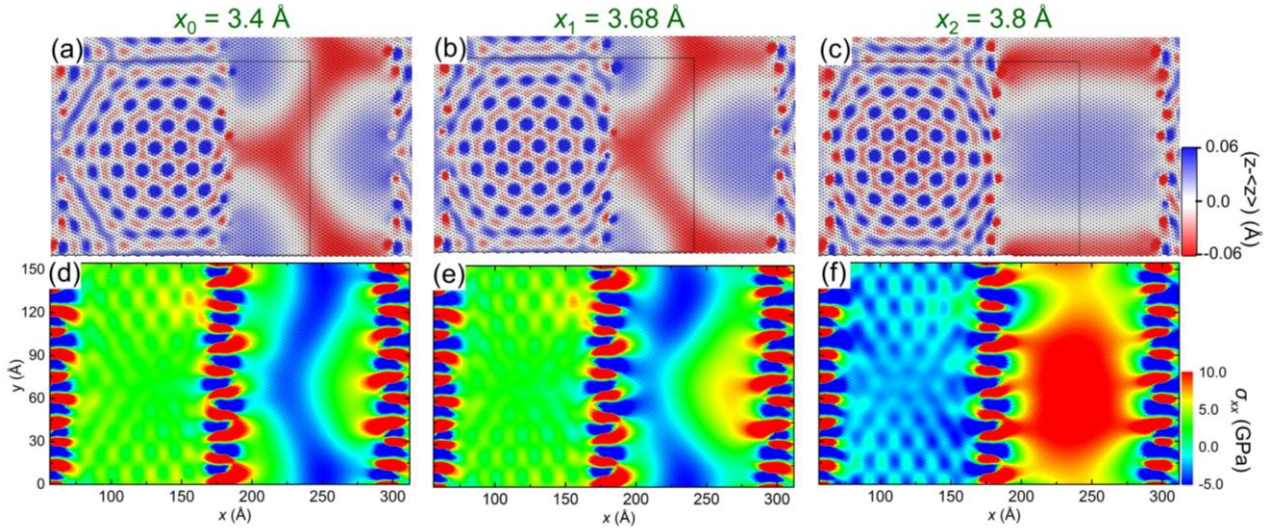

FIG. S16. Out of plane corrugation (a)-(c) of several moiré superstructures snapshots and the corresponding lateral stress maps (d)-(f) along the sliding (*x*) direction. The results were obtained during quasistatic simulation performed under a normal load of 2.9 GPa.

In Fig. 4(c)-4(d) of the main text, we presented the interlayer and intralayer energy components profiles for this system, respectively, obtained via quasistatic simulations, which demonstrate that sharp energy variations occur during moiré superstructure stick-slip motion under high normal load. In Fig. S17 we provide the corresponding total potential energy profiles, demonstrating that under a normal load of 2.9 GPa, the sliding energy barrier increases by ~ 1.6 eV with respect to the load-free case. This, in turn, leads to stronger in-plane stress accumulation and eventual release under high normal load, giving rise to higher energy dissipation.

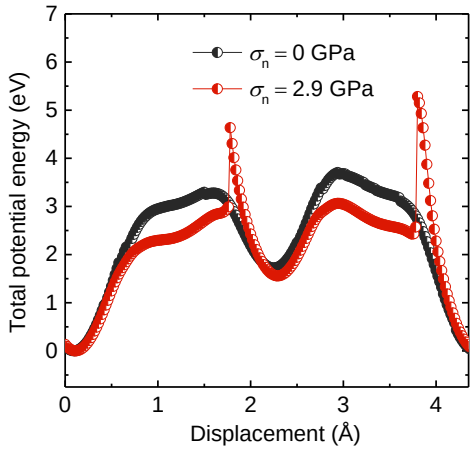

FIG. S17. Quasistatic total potential energy as a function of slider displacement under zero normal load (black) and a normal load of 2.9 GPa (red). These diagrams are the sums of the inter- and intralayer contributions appearing in panels (c) and (d) of Fig. 4 of the main text, respectively.

7.2. Stress evolutions for quasistatic simulations and dynamic simulations at $v_0 = 0.2$ m/s

In Fig. 5 of the main text, we presented an in-plane stress evolution analysis for a high slider velocity of v_0 = 5 m/s. For completeness, we present in Fig. S18 similar results obtained during quasistatic calculations and low velocity ($v_0 = 0.2$ m/s) simulations under a normal load of 2.9 GPa and zero temperature. Similar to the high sliding velocity case, clear stick slip motion is observed both in the quasistatic and the low-velocity simulations. Due to the quasi-static simulation procedure the former (Fig. S18(a)) does not exhibit high-frequency features following slip events (See Supplementary Movie 2). The latter, however, does feature multiple wave reflections between the two GBs (Fig. S18(b)), however considerably less pronounced than in the

high slider velocity case (see Fig. 5 of the main text), with reduced impact on the overall friction due to the overall lower kinetic energy of the system.

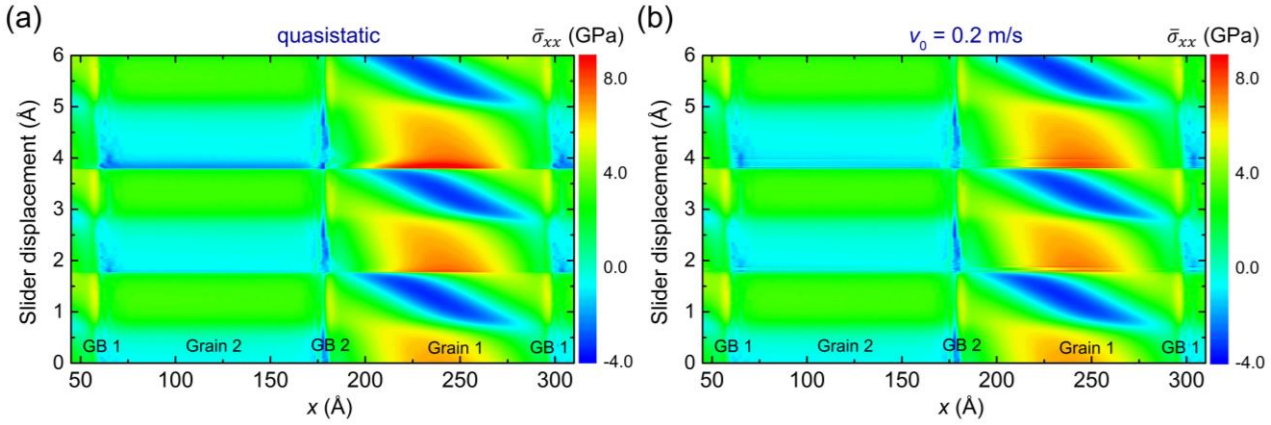

FIG. S18. Two-dimensional PolyGr stress evolution maps. (a) In-plane stress map along the sliding direction as a function of slider displacement obtained via quasistatic calculations. (b) Same as (a) but for dynamic calculations with a slider velocity of $v_0 = 0.2\ \mathrm{m/s}$. The calculations are performed at zero temperature and under a normal load of 2.9 GPa. In both maps, the stress is averaged along the direction perpendicular to the sliding path (y). Positive and negative values indicate expansion and compressive stresses, respectively.

7.3. Stress Propagation Speed at the Moiré Instability

As discussed in the main text, the propagation velocity of the incident and reflected waves induced by the stick-slip instability can be estimated from the slope of the wave-fronts in the stress evolution maps. In Fig. S19(a) we demonstrate such calculations for the case of a slider velocity of $v_0 = 5$ m/s and a normal load of 2.9 GPa. Both incident and reflection wave front velocities are found to increase with the applied normal load (Fig. S19(b)). The kinetic energy associated with these two waves are proportional to $E_{\mathrm{T}}^{\mathrm{in}} \propto (v_{\mathrm{in}} - v_{\mathrm{m}})^2$ and $E_T^{\mathrm{re}} \propto (v_{\mathrm{re}} + v_{\mathrm{m}})^2$, where we have taken into account that the former travels against the sliding direction, whereas the latter travels in the sliding direction. This excess kinetic energy is dissipated during sliding. Fig. S19(c) shows that the sum of these contributions follows nicely the calculated energy dissipation, thus further demonstrating that a major contribution to the friction originates from the in-plane motion of the high-frequency multiply reflecting waves induced by the slip events. At a sliding velocity of 5 m/s, this contribution is estimated to be ~50%, compared to the quasistatic results of Fig. 3(a) of the main text.

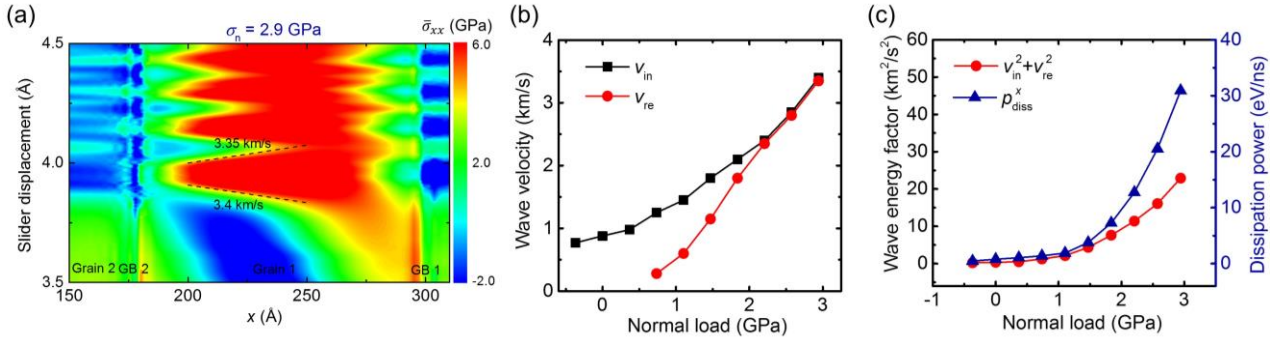

FIG. S19. Evaluation of the propagation velocity of the incident and reflected waves induced by the stick-slip instability. (a) An example of wave velocity estimation from the lateral stress evolution map. (b) The incident and reflection wave velocities as a function of normal load. (c) Wave energy as a function of normal load (red, left vertical axis) compared to the power dissipation in the sliding direction (blue, right vertical axis).

References:

[1] D. W. Brenner, O. A. Shenderova, J. A. Harrison, S. J. Stuart, B. Ni, and S. B. Sinnott, *A second-generation reactive empirical bond order (REBO) potential energy expression for hydrocarbons*, J. Phys.: Condens. Matter **14**, 783 (2002).

[2] J. Tersoff, *New empirical approach for the structure and energy of covalent systems*, Phys. Rev. B **37**, 6991 (1988).

[3] D. Mandelli, W. Ouyang, O. Hod, and M. Urbakh, *Negative Friction Coefficients in Superlubric Graphite--Hexagonal Boron Nitride Heterojunctions*, Phys. Rev. Lett. **122**, 076102 (2019).

[4] X. Gao, W. Ouyang, M. Urbakh, and O. Hod, *Superlubric polycrystalline graphene interfaces*, Nat. Commun. **12**, 5694 (2021).

[5] X. Gao, W. Ouyang, O. Hod, and M. Urbakh, *Mechanisms of frictional energy dissipation at graphene grain boundaries*, Phys. Rev. B **103**, 045418 (2021).

[6] S. Tang, H. Wang, Y. Zhang, A. Li, H. Xie, X. Liu, L. Liu, T. Li, F. Huang, X. Xie *et al.*, *Precisely aligned graphene grown on hexagonal boron nitride by catalyst free chemical vapor deposition*, Sci. Rep. **3**, 2666 (2013).

[7] D. Mandelli, W. Ouyang, M. Urbakh, and O. Hod, *The Princess and the Nanoscale Pea: Long-Range Penetration of Surface Distortions into Layered Materials Stacks*, ACS Nano **13**, 7603 (2019).

[8] S. Plimpton, *Fast Parallel Algorithms for Short-Range Molecular Dynamics*, J. Comput. Phys. **117**, 1 (1995).

[9] A. N. Kolmogorov and V. H. Crespi, *Registry-dependent interlayer potential for graphitic systems*, Phys. Rev. B **71**, 235415 (2005).

[10] I. Leven, I. Azuri, L. Kronik, and O. Hod, *Inter-layer potential for hexagonal boron nitride*, J. Chem. Phys. **140**, 104106 (2014).

[11] I. Leven, T. Maaravi, I. Azuri, L. Kronik, and O. Hod, *Interlayer Potential for Graphene/h-BN Heterostructures*, J. Chem. Theory Comput. **12**, 2896 (2016).

[12] T. Maaravi, I. Leven, I. Azuri, L. Kronik, and O. Hod, *Interlayer Potential for Homogeneous Graphene and Hexagonal Boron Nitride Systems: Reparametrization for Many-Body Dispersion Effects*, J. Phys. Chem. C **121**, 22826 (2017).

[13] W. Ouyang, D. Mandelli, M. Urbakh, and O. Hod, *Nanoserpents: Graphene Nanoribbon Motion on Two-Dimensional Hexagonal Materials*, Nano Lett. **18**, 6009 (2018).

[14] O. V. Yazyev and S. G. Louie, *Topological defects in graphene: Dislocations and grain boundaries*, Phys. Rev. B **81**, 195420 (2010).

[15] J. Červenka and C. F. J. Flipse, *Structural and electronic properties of grain boundaries in graphite: Planes of periodically distributed point defects*, Phys. Rev. B **79**, 195429 (2009).

[16] Y. Tison, J. Lagoute, V. Repain, C. Chacon, Y. Girard, F. Joucken, R. Sporken, F. Gargiulo, O. V. Yazyev, and S. Rousset, *Grain Boundaries in Graphene on SiC(000$\bar{1}$) Substrate*, Nano Lett. **14**, 6382 (2014).

[17] E. Bitzek, P. Koskinen, F. Gähler, M. Moseler, and P. Gumbsch, *Structural Relaxation Made Simple*, Phys. Rev. Lett. **97**, 170201 (2006).

[18] J. Guénolé, W. G. Nöhring, A. Vaid, F. Houllé, Z. Xie, A. Prakash, and E. Bitzek, *Assessment and optimization of the fast inertial relaxation engine (fire) for energy minimization in atomistic simulations and its implementation in lammps*, Comput. Mater. Sci. **175**, 109584 (2020).

[19] I. Leven, R. Guerra, A. Vanossi, E. Tosatti, and O. Hod, *Multiwalled nanotube faceting unravelled*, Nat. Nanotechnol. **11**, 1082 (2016).
[20] I. Leven, D. Krepel, O. Shemesh, and O. Hod, *Robust Superlubricity in Graphene/h-BN Heterojunctions*, J. Phys. Chem. Lett. **4**, 115 (2013).